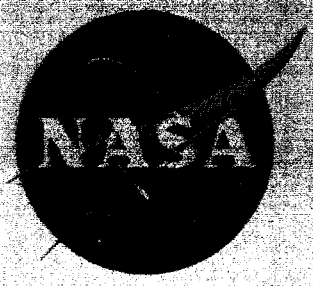

TECHNICAL MEMORANDUM

X-702

PRESSURE DISTRIBUTIONS ON A FLAT-PLATE DELTA WING SWEPT 65° AT A MACH NUMBER OF 5.97 AT ANGLES OF ATTACK FROM 65° TO 115° AND ANGLES OF ROLL FROM 0° TO 25° AT A 90° ANGLE OF ATTACK

By Theodore J. Goldberg and James G. Hondros

Langley Research Center
Langley Station, Hampton, Va.

NATIONAL AERONAUTICS AND SPACE ADMINISTRATION
WASHINGTON
August 1962

NATIONAL AERONAUTICS AND SPACE ADMINISTRATION

TECHNICAL MEMORANDUM X-702

PRESSURE DISTRIBUTIONS ON A FLAT-PLATE DELTA WING SWEPT 65° AT A MACH NUMBER OF 5.97 AT ANGLES OF ATTACK FROM 65° TO 115° AND ANGLES OF ROLL FROM 0° TO 25° AT A 90° ANGLE OF ATTACK*

By Theodore J. Goldberg and James G. Hondro[redacted]

33327

SUMMARY

Pressure distributions on a flat-plate delta wing swept 65° with squared leading and trailing edges and sharp corners were obtained at a Mach number of 5.97 and a Reynolds number of 2.3×10^6 through an angle-of-attack range of 65° to 115° and at angles of roll from 0° to 25° at a 90° angle of attack. The results of this investigation indicate the existence of stagnation pressure on the lower surface at all angles of attack with the possible exception of 65°. At angles of attack from 80° to 100°, the stagnation point shifted from 15 to 85 percent of the root chord. At an angle of attack of 90°, as the roll angle increased, the stagnation point moved toward the trailing edge and the upstream wing tip; at a roll angle of 0°, the stagnation point was located on the mid-span at 67 percent of the root chord; and at a 25° angle of roll it was located at 90 percent of the root chord and 85 percent of the semispan. At an angle of attack of 100°, the pressure distributions along the first two-thirds of the chords indicate nearly constant pressure relief along the leading edge. At angles of attack other than 100°, the distributions indicate that the leading-edge pressure relief varies with angle of attack, with the greatest variation at the lower angles. The pressure relief along the last 10 percent of the root chord at each angle of attack is almost constant. A correlation of the ratio of local to maximum pressure coefficients as a function of a nondimensionalized distance from the centroid of the model at a 90° angle of attack indicates a nearly constant pressure distribution along all rays emanating from the centroid of the wing surface with the exception of the trailing-edge corner. Comparisons with data obtained on flat-faced cylinders indicate that pressure distributions at 90° angle of attack are essentially unaffected by changing from a delta to a circular planform. The predictions of normal-force coefficient at various angles of attack and roll made by using modified Newtonian theory did not agree with test results except around 70° and 110° angles of attack and at an angle of roll of about 16°.

*Title, Unclassified.

[redacted] Author

[redacted]

INTRODUCTION

The use of Newtonian and modified Newtonian theories has proved to be of value in the prediction of forces on bodies at hypersonic velocities (ref. 1, for example). However, there are no known exact theories to predict the pressure distributions on flat-plate bodies (such as the delta wing) at angles of attack greater than those for shock detachment at hypersonic Mach numbers. In addition, the dearth of experimental data in this area has inhibited the development of a theoretical or empirical method of accurately predicting the pressure distributions on such bodies. [redacted]efore, an investigation has been initiated at the NASA Langley Research [redacted] in detailed pressure measurements for delta wings over a wide [redacted]ach numbers and angles of attack. Some of the recent results can be found in references 2 to 5.

The purpose of this paper is to present detailed pressure distributions on the pressure surface of a 1/8-inch-thick, flat-plate delta wing swept 65° with a 4.00-inch root chord at a Mach number of 5.97 and angles of attack from 65° to 115° and at angles of roll from 0° to 25° at a 90° angle of attack. This investigation was carried out in the Langley 20-inch Mach 6 tunnel at a Reynolds number of 2.3×10^6 based upon the root chord.

SYMBOLS

$b/2$ maximum semispan, in.

C_N normal-force coefficient, $F_N/q_\infty S$

$C_{N,90^\circ}$ normal-force coefficient in roll at a 90° angle of attack

$$C_p = \frac{p_l - p_\infty}{q_\infty}$$

$$C_{p,max} = \frac{p_{t,2} - p_\infty}{q_\infty}$$

c chord, in.

c_r root chord, in.

F_N normal force, lb

[redacted]

L	length of leading edge of wing, in.
M	free-stream Mach number
p_∞	free-stream static pressure, lb/sq in. abs
p_l	local measured pressure on body, lb/sq in. abs
$p_{t,2}$	stagnation pressure behind normal shock, lb/sq in. abs
q_∞	free-stream dynamic pressure, lb/sq in. abs
r	radial length from model centroid, in.
S	planform area, sq in.
s	distance along ray or chord, in.
x,y	body-axis system of coordinates (see table I)
α	angle of attack, deg
ϕ	angle of roll, deg

APPARATUS AND METHODS

This investigation was conducted in the Langley 20-inch Mach 6 tunnel. The tunnel, which has been described in reference 6, is a blowdown-to-atmosphere type capable of operation at a maximum stagnation pressure of 580 pounds per square inch absolute and a maximum stagnation temperature of 600° F. The air is dried by an activated alumina dryer designed to provide a dewpoint temperature of -40° F at 600 pounds per square inch absolute.

The model was supported in the tunnel by the gooseneck support system shown in figure 1, which pitched the model in the horizontal plane. This support system provided an angle-of-attack range of 50°. The models were mounted with the upper surface normal to the center line of the sting; this resulted in a model angle-of-attack range from 65° to 115°. A 90° rotation of the model on the sting permitted tests at roll angles of 0° to 25° at a 90° angle of attack.

The angles of attack and roll were measured mechanically by a counter geared to the vertical shaft of the support system. All model pressures were recorded by photographing a multiple-tube mercury manometer. Tunnel

stagnation pressures were measured with a Bourdon gage calibrated from 0 to 600 pounds per square inch.

The tests were conducted at a stagnation pressure of 365 pounds per square inch absolute and a temperature of 400° F which yielded a model Reynolds number of 2.3×10^6 based on root chord.

MODEL

The model used in this investigation was a 1/8-inch-thick, flat-plate delta wing swept 65° with a root chord of 4.00 inches, a span of 3.73 inches, squared leading and trailing edges, and sharp corners. The model orifices had inside diameters of 0.013 inch connected just behind the model to tubing with an inside diameter of 0.070 inch. All model dimensions and orifice locations are given in table I. A photograph of the model is shown in figure 2.

DATA REDUCTION AND ACCURACY

Due to the symmetry of the model, the pressures measured at orifices having the same locations on each side of the root chord were averaged and the results are presented for only one-half of the model at various angles of attack. Since the Mach number in the tunnel is known to vary with time, in order to obtain better accuracy the Mach number at each angle of attack and roll position was determined by assuming that the maximum faired value of the measured pressure ratios (ratio of local pressure on the model to tunnel stagnation pressure) was equal to the total pressure ratio across a normal shock. In order to obtain pressure distributions over the windward surface of the model, pressures along all rays shown in table I were cross-faired so that the value at each intersection was the same for all curves through that point. Normal-force coefficients were obtained by first integrating along each chord line and then integrating in the spanwise direction.

The Mach number for this investigation was 5.97 ± 0.02. The estimated maximum error of measurement of each local-pressure point and the stagnation pressure is 0.5 percent of the maximum measured value. Model alinement and angles of attack and roll are believed to be accurate to $\pm 0.5°$.

RESULTS AND DISCUSSION

Typical schlieren photographs of the model in the angle-of-attack and roll attitudes are shown in figure 3 to indicate the shape of the shock. Pressure distributions (in terms of the ratio of the local pressure on the windward surface to the free-stream static pressure) along several chord lines, leading and trailing edges, and radial rays emanating from the orifice nearest the apex and from the center of gravity of the model are presented in figures 4 to 8 for angles of attack from 65° to 115° and for angles of roll from 0° to 25° at a 90° angle of attack. In addition, the normal-force coefficients obtained by integration of the pressures over the windward surface are compared in figure 9 with those obtained from the force measurements of reference 7.

L
1
6
1
3

Angle of Attack

The overall pressure distribution can best be seen in figure 4(a), which shows the chordwise distributions at four evenly spaced semispanwise stations where the chordwise distances have been nondimensionalized on the basis of individual chord lengths. The pressure distributions along the center line of the wing (maximum chord) reveal that only at an angle of attack of 65° was there no clearly defined peak. Therefore, it cannot be definitely established whether or not a stagnation point was measured at this attitude. However, since the maximum measured value does yield a Mach number within the known range of the tunnel, it was considered to be the stagnation value. At all the other angles of attack of the tests, the stagnation pressure was definitely measured and found to move rearward to very near the trailing edge with increasing angle of attack. A curve of the chordwise stagnation-point shift is presented in figure 10, which shows that for a change in angle of attack from 80° to 100°, the stagnation point moves from 15 percent to 85 percent of the maximum chord.

The general slope of the pressure distribution along the center line (fig. 4(a)) can be seen to vary from negative to positive with increasing angle of attack, as expected. However, the absolute magnitudes of the slopes at angles of attack above 90° are greater than those for the comparable angles of attack below 90° (for example, $\alpha = 110°$ compared with $\alpha = 70°$) except at the leading and trailing edges. This result illustrates the greater relief afforded at the nose for $\alpha > 90°$ than at the trailing edge for $\alpha < 90°$. Nevertheless, figure 9 shows that the normal-force-coefficient curve is nearly symmetrical about $\alpha = 90°$, within experimental accuracy (results of force data of ref. 2 are symmetrical), as a result of the area distribution over which these pressures act. The uniform value of pressure ratio predicted by modified Newtonian theory for each angle of attack is indicated by tick marks at

the right side of figure 4(a). At $\alpha = 90^\circ$, the predicted pressure agrees with the measured value only at the stagnation region. At all other points the measured pressures are naturally lower because of the relieving effects and, therefore, the predicted normal force is higher, as seen in figure 9. At all other angles of attack of the investigation the predicted pressures are lower than stagnation pressure, and since a stagnation value was measured, there are regions of higher pressure. In addition, the relieving effects result in regions of lower pressure. Therefore, the predicted value of the normal-force coefficient approaches the measured value until at some angle of attack they are equal. For the delta wing tested, this occurs at angles of attack of about 70° and 110°, as seen in figure 9. With a further divergence from $\alpha = 90^\circ$, the predicted value of normal-force coefficient becomes lower than the measured value.

In general, the chordwise distributions for the other three semispanwise stations shown in figure 4(a) have trends similar to the distribution along the center line. This is especially true at the higher angles of attack. At an angle of attack of 100°, the pressure distributions over the first two-thirds of the four chord lines fall almost on a single line, indicating that the pressure relief all along the leading edge must be about the same. However, with increasing divergence in angle of attack from $\alpha = 100^\circ$, there is an increasing divergence in the distributions for the four chord lines, with the greatest difference occurring at the lowest angles of attack. Thus, the relief along the leading edge varies inversely with angle of attack. From about 66 percent to 100 percent of the chord, it can be seen in figure 4(a) that the pressure distributions along the four chord lines indicate similar trends of pressure drop at each angle of attack. It can further be seen from figures 4(a) and 6(a) that the pressure relief along the last 10 percent of the root chord (at the trailing edge) at each angle of attack is almost constant, and only the magnitude of the pressure is changed with angle-of-attack variation.

A more detailed picture of the pressure distributions along three rays parallel to the leading edge is presented in figure 5(a). At each value of s, the differences between the pressure ratios at the three rays are approximately constant except near the model nose at the extremities of the angle-of-attack range. The approximate value of the difference in p_l/p_∞ between the most outboard and inboard rays is about 5. At a 90° angle of attack the pressure along each ray remains nearly constant and supports the isobar concept of reference 3.

Figure 7(a) is a radial pressure distribution emanating from the apex orifice of the model. As shown in the figure, the greatest deviation from the root-chord distribution occurs along the leading edge, while the root chord and the intermediate distribution remain about the same. The tick marks on the right of the figure indicate the constant pressure level predicted by modified Newtonian theory at each angle of attack.

A correlation of the ratio of local to maximum pressure coefficients as a function of a nondimensionalized distance from the centroid of the model at a 90° angle of attack is presented in figure 8. The distances were nondimensionalized by dividing the distance along each ray by the total length of the ray. The prime indication of the correlation is the existence of nearly similar pressure distribution along all rays emanating from the centroid with the exception of the ray to the trailing-edge corner. The existence of this exception was verified by measurements along rays to both trailing-edge corners at the 90° angle-of-attack position in the angle-of-attack and angle-of-roll attitudes. A further comparison with data from reference 8 and unpublished data at a Mach number of 5.95 on a flat, square-planform plate and at a Mach number of 8 on a flat-faced disk with a converging 30° afterbody indicate essentially no differences between the pressure distributions resulting from planform variations at a 90° angle of attack. In addition, a curve from the empirical equation of reference 9 is seen to be in very good agreement with the data. This curve was obtained from data for Mach numbers of 2.0 to 5.8.

Angle of Roll

The effects of roll angle at a 90° angle of attack are presented in figures 4(b), 5(b), 6(b), and 7(b). The pressure distributions along equally spaced chord lines are shown in figure 4(b). As seen in figure 4(b), the nondimensionalized slopes and trends of the curves remain about the same with increasing angle of roll, while the pressure distributions separate themselves in an orderly manner from the upstream wing tip to the downstream tip, with the highest pressure occurring on the upstream side. The maximum difference in pressure along the span at 50 percent of the chords is about 4 times as great at 25° roll angle as at 0° roll.

A stagnation point was found on one of the chord lines at all roll angles of the tests. The movement of the stagnation point obtained from interpolation of the chordwise pressure distributions at four semispanwise stations is presented in figure 11 in terms of percent root chord and percent maximum semispan. With increasing roll angle (up to 25°), the stagnation point moves toward the trailing edge from about 67 percent to 90 percent of the root chord as it moves from the root chord to about 85 percent of the maximum upstream semispan.

Leading-edge pressure relief as a function of roll angle can be seen in figure 5(b). As might be expected, the curves indicate that the upstream leading edge affords less pressure relief than the downstream edge because of the stagnation-point movement and the acceleration of flow from the stagnation point to the wing tip across the model face. The pressure relief on the downstream wing tip of the model increases with increasing roll angle.

Figure 6(b) shows the trailing-edge pressure relief over the range of roll angles of the tests. The variation in pressure difference between trailing-edge stations along a chord line remains about constant, while the spanwise variation of pressure from wing tip to wing tip increases with increasing angle of roll at a 90° angle of attack.

A radial pressure distribution emanating from the apex orifice of the model is presented in figure 7(b). It can be seen that the effects of angle of roll are most pronounced near the edges, while the internal distributions are relatively unaffected up to and inclusive of 10° roll. Above 10° roll, the internal spread increases with increasing angle of roll.

The normal-force coefficients over the range of roll angles of the tests were obtained by integrating the pressures and are shown in figure 9(b). The agreement with the force data of reference 7 is excellent. As in the case of angle of attack, the $C_{N,90^\circ}$ agrees with the modified Newtonian theory at only one point, $\phi = 16^\circ$, because modified Newtonian theory predicts stagnation pressure at only 0° angle of roll. Below $\phi = 16^\circ$, modified Newtonian theory overpredicts $C_{N,90^\circ}$; and above $\phi = 16^\circ$, it underpredicts $C_{N,90^\circ}$.

CONCLUSIONS

The results of a pressure-distribution investigation at a Mach number of 5.97 on a flat-plate delta wing swept 65° through an angle-of-attack range of 65° to 115° and angle-of-roll range of 0° to 25° at a 90° angle of attack indicate the following:

1. A stagnation point was measured on the model at all angles of attack with the possible exception of 65°. At angles of attack from 80° to 100°, the stagnation point shifted from 15 to 85 percent of the root chord. At an angle of attack of 90°, as the roll angle increased, the stagnation point moved toward the trailing edge and the upstream wing tip; at a roll angle of 0°, the stagnation point was located on the midspan at 67 percent of the root chord; and at a 25° angle of roll it was located at 90 percent of the root chord and 85 percent of the upstream semispan.

2. At 100° angle of attack the pressure distributions along the first two-thirds of the chords indicate a nearly constant pressure relief along the leading edge. A deviation from a 100° angle of attack causes the chordwise distributions to diverge, with the greatest difference occurring at the lowest angles of attack. The pressure relief along the leading edge thus varies inversely with angle of attack, while the pressure

relief along the last 10 percent of the root chord (at the trailing edge) at each angle of attack is almost constant.

3. A nondimensionalized correlation of the ratio of distances emanating from the centroid of the model and local pressure ratios obtained at a 90° angle of attack indicates the existence of nearly constant pressure distribution over the wing surface with exception of the trailing-edge corner. Comparison with data obtained on square-, triangular-, and circular-planform models at Mach numbers from 4.95 to 8.0 indicates essentially no difference between the radial-pressure distributions.

L
1
6
1
3

4. The normal-force coefficient predicted by modified Newtonian theory agrees with the value obtained by integrating the measured pressures at 70° and 110° angles of attack because the higher measured pressures compensate for the lower pressures resulting from edge relief. In the roll positions, at an angle of attack of 90° the agreement of the normal-force coefficient with theory is obtained at an angle of roll of about 16°.

Langley Research Center,
National Aeronautics and Space Administration,
Langley Station, Hampton, Va., June 4, 1962.

[redacted]

REFERENCES

1. Rainey, Robert W.: Working Charts for Rapid Prediction of Force and Pressure Coefficients on Arbitrary Bodies of Revolution by Use of Newtonian Concepts. NASA TN D-176, 1959.

2. Bertram, Mitchel H., and Henderson, Arthur, Jr.: Recent Hypersonic Studies of Wings and Bodies. ARS Jour., vol. 31, no. 8, Aug. 1961, pp. 1129-1139.

3. Bertram, Mitchel H., Feller, William V., and Dunavant, James C.: Flow Fields, Pressure Distributions, and Heat Transfer for Delta Wings at Hypersonic Speeds. NASA TM X-316, 1960.

4. Mueller, James N. (with appendix by Eugene S. Love): Pressure Distributions on Blunt Delta Wings at a Mach Number of 2.91 and Angles of Attack up to 90°. NASA TM X-623, 1962.

5. Dunavant, James C.: Investigation of Heat Transfer and Pressures on Highly Swept Flat and Dihedraled Delta Wings at Mach Numbers of 6.8 and 9.6 and Angles of Attack to 90°. NASA TM X-688, 1962.

6. Ashby, George C., Jr., and Fitzgerald, Paul E., Jr.: Longitudinal Stability and Control Characteristics of Missile Configurations Having Several Highly Swept Cruciform Fins and a Number of Trailing-Edge and Fin-Tip Controls at Mach Numbers From 2.21 to 6.01. NASA TM X-335, 1961.

7. Hondros, James G., and Goldberg, Theodore J.: Aerodynamic Characteristics of a Group of Winged Reentry Vehicles at Mach Number 6.01 at Angles of Attack From 60° to 120° and -10° to 30° Roll at 90° Angle of Attack. NASA TM X-511, 1961.

8. Cooper, Morton, and Mayo, Edward E.: Measurements of Local Heat Transfer and Pressure on Six 2-Inch-Diameter Blunt Bodies at a Mach Number of 4.95 and at Reynolds Numbers Per Foot Up to 81×10^6. NASA MEMO 1-3-59L, 1959.

9. Dugan, Duane W.: Estimation of Static Longitudinal Stability of Aircraft Configurations at High Mach Numbers and at Angles of Attack Between 0° and ±180°. NASA MEMO 1-17-59A, 1959.

[redacted]

TABLE I.- MODEL ORIFICE DIMENSIONS AND LOCATIONS

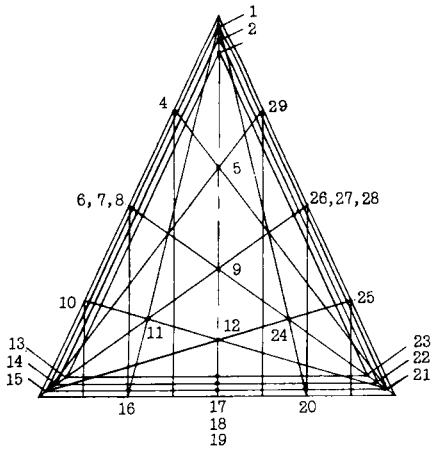

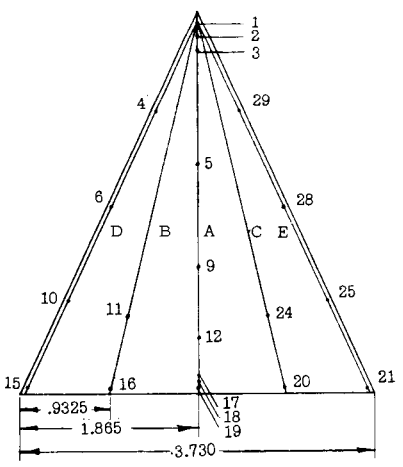

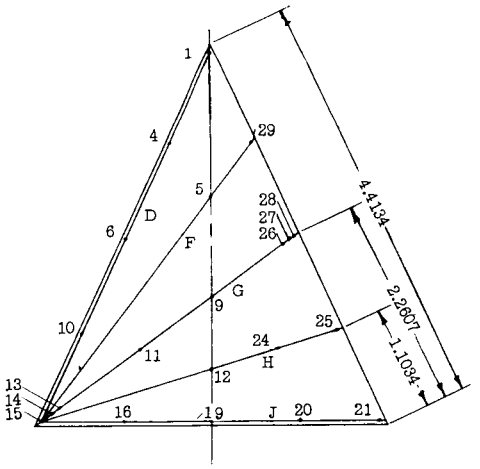

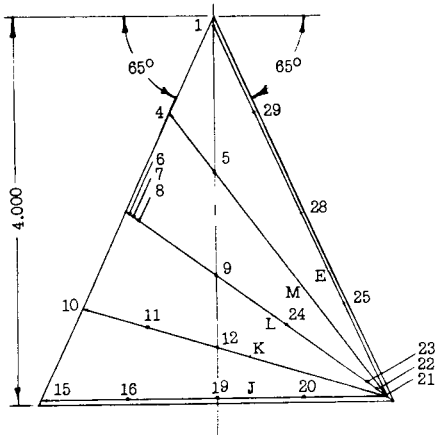

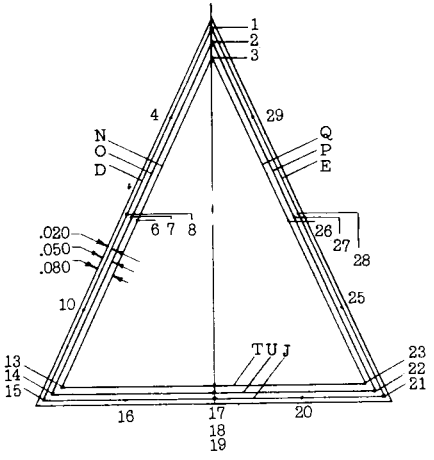

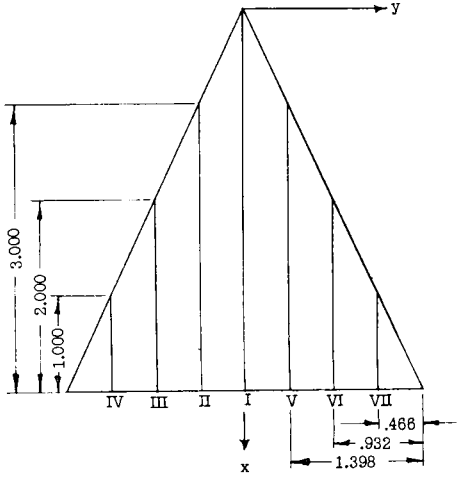

Ray	Orifice	Intersection point	y, in.	x, in.	Distance along ray, in.
A	1		0	0.047	0
	2			.118	.071
	3			.189	.142
	5			1.604	1.557
	9			2.667	2.620
	12			3.423	3.376
	17			3.905	3.858
	18			3.941	3.893
	19		↓	3.976	3.928
B	1		0	.047	0
		B-O	-.034	.191	.148
		B-N	-.068	.335	.295
		B-M	-.281	1.240	1.225
		B-II	-.466	2.024	2.031
		B-L	-.529	2.289	2.303
	11		-.744	3.199	3.238
		B-H	-.858	3.682	3.735
		B-T	-.910	3.905	3.964
		B-U	-.919	3.941	4.001
	16		-.927	3.976	4.037
C	1		0	.047	0
		C-P	.034	.191	.148
		C-Q	.068	.335	.295
		C-F	.281	1.240	1.225
		C-V	.466	2.024	2.031
		C-G	.529	2.289	2.303
	24		.744	3.199	3.238
		C-K	.858	3.682	3.735
		C-T	.910	3.905	3.964
		C-U	.919	3.941	4.001
	20		.927	3.976	4.037
D	1		0	.047	0
	4		-.453	1.018	1.071
		D-II	-.466	1.048	1.103
	6		-.916	2.012	2.168
		D-III	-.933	2.048	2.207
	10		-1.380	3.006	3.264
		D-IV	-1.399	3.047	3.310
	15		-1.832	3.976	4.335
E	1		0	.047	0
	29		.453	1.018	1.071
		E-V	.466	1.048	1.103
	28		.916	2.012	2.168
		E-VI	.933	2.048	2.207
	25		1.380	3.006	3.264
		E-VII	1.399	3.047	3.310
	21		1.832	3.976	4.335
O	2		0	.118	.064
		O-B	-.034	.191	.144
		O-M	-.432	1.045	1.086
		O-II	-.466	1.119	1.167
	7		-.891	2.030	2.173
		O-III	-.933	2.119	2.271
		O-K	-1.351	3.015	3.260
		O-IV	-1.399	3.118	3.374
		O-F	-1.748	3.868	4.202
	14		-1.782	3.941	4.282
N	3		0	.189	.129
		N-B	-.068	.335	.290
		N-M	-.411	1.071	1.102
		N-II	-.466	1.190	1.233
	8		-.867	2.047	2.179
		N-III	-.933	2.190	2.336
		N-K	-1.322	3.023	3.256
		N-IV	-1.399	3.189	3.439
		N-F	-1.665	3.760	4.069
	13		-1.733	3.905	4.229

Ray	Orifice	Intersection point	y, in.	x, in.	Distance along ray, in.
P	2		0	0.118	0.064
		P-C	.034	.191	.144
		P-F	.432	1.045	1.086
		P-V	.466	1.119	1.167
	27		.891	2.030	2.173
		P-VI	.933	2.119	2.271
		P-H	1.351	3.015	3.260
		P-VII	1.399	3.118	3.374
		P-M	1.748	3.868	4.202
	22		1.782	3.941	4.282
Q	3		0	.189	.129
		Q-C	.068	.335	.290
		Q-F	.411	1.071	1.102
		Q-V	.466	1.190	1.233
	26		.867	2.047	2.179
		Q-VI	.933	2.190	2.336
		Q-H	1.322	3.023	3.256
		Q-VII	1.399	3.189	3.439
		Q-M	1.665	3.760	4.069
	23		1.733	3.905	4.229
J	15		-1.832	3.976	0
		J-IV	-1.399	↓	.433
		J-III	-.933		.899
	16		-.927		.905
		J-II	-.466		1.366
	19		0		1.832
		J-V	.466		2.298
	20		.927		2.759
		J-VI	.933		2.764
		J-VII	1.399		3.231
	21		1.832	↓	3.664
U	14		-1.782	3.941	.050
		U-H	-1.715		.118
		U-IV	-1.399		.434
		U-III	-.933		.900
		U-B	-.919		.914
		U-II	-.466		1.366
	18		0		1.832
		U-V	.466		2.298
		U-C	.919		2.750
		U-VI	.933		2.764
		U-VII	1.399		3.230
		U-K	1.715		3.546
	22		1.782	↓	3.614
T	13		-1.733	3.905	.099
		T-H	-1.598		.234
		T-IV	-1.399		.433
		T-III	-.933		.899
		T-B	-.910		.921
		T-II	-.466		1.365
	17		0		1.832
		T-V	.466		2.298
		T-C	.910		2.742
		T-VI	.933		2.764
		T-VII	1.399		3.230
		T-K	1.598		3.429
	23		1.733	↓	3.564
F	15		-1.832	3.976	0
		F-O	-1.748	3.868	.137
		F-N	-1.665	3.760	.274
		F-IV	-1.399	3.415	.709
		F-K	-1.139	3.078	1.134
		F-III	-.933	2.812	1.472
		F-L	-.529	2.289	2.132
		F-II	-.466	2.208	2.235
	5		0	1.604	2.997
		F-C	.281	1.240	3.458
		F-Q	.411	1.071	3.670
		F-P	.432	1.045	3.704
	29		.453	1.018	3.738

Ray	Orifice	Intersection point	y, in.	x, in.	Distance along ray, in.
G	15		-1.832	3.976	0
	14		-1.782	3.941	.061
	13		-1.733	3.905	.122
		G-IV	-1.399	3.667	.532
		G-III	-.933	3.333	1.106
	11		-.744	3.199	1.338
		G-II	-.466	3.000	1.679
	9		0	2.667	2.252
		G-V	.466	2.357	2.825
		G-M	.529	2.289	2.902
	26		.867	2.047	3.317
	27		.891	2.030	3.347
	28		.916	2.012	3.378
H	15		-1.832	3.976	0
		H-J	-1.715	3.941	.122
		H-T	-1.598	3.905	.245
		H-IV	-1.399	3.845	.453
		H-III	-.933	3.704	.940
		H-B	-.858	3.682	1.018
		H-II	-.466	3.563	1.427
	12		0	3.423	1.914
		H-V	.466	3.281	2.401
	24		.744	3.199	2.691
		H-VI	.933	3.140	2.888
		H-M	1.139	3.078	3.104
		H-Q	1.322	3.023	3.294
		H-P	1.351	3.015	3.324
	25		1.380	3.006	3.355
K	21		1.832	3.976	0
		K-U	1.715	3.941	.122
		K-T	1.598	3.905	.245
		K-VII	1.399	3.845	.453
		K-VI	.933	3.704	.940
		K-C	.858	3.682	1.018
		K-V	.466	3.563	1.427
	12		0	3.423	1.914
		K-II	-.466	3.281	2.401
	11		-.744	3.199	2.691
		K-III	-.933	3.140	2.888
		K-F	-1.139	3.078	3.104
		K-N	-1.322	3.023	3.294
		K-O	-1.351	3.015	3.324
	10		-1.380	3.006	3.355
L	21		1.832	3.976	0
	22		1.782	3.941	.061
	23		1.733	3.905	.122
		L-VII	1.399	3.667	.532
		L-VI	.933	3.333	1.106
	24		.744	3.199	1.338
		L-V	.466	3.000	1.679
	9		0	2.667	2.252
		L-II	-.466	2.357	2.825
		L-F	-.529	2.289	2.902
	8		-.867	2.047	3.317
	7		-.891	2.030	3.347
	6		-.916	2.012	3.378
M	21		1.832	3.976	0
		M-P	1.748	3.868	.137
		M-Q	1.665	3.760	.274
		M-VII	1.399	3.415	.709
		M-H	1.139	3.078	1.134
		M-VI	.933	2.812	1.472
		M-O	.529	2.289	2.132
		M-V	.466	2.208	2.235
	5		0	1.604	2.997
		M-B	-.281	1.240	3.458
		M-N	-.411	1.071	3.670
		M-O	-.432	1.045	3.704
	4		-.453	1.018	3.738

Spanwise station	Orifice	Intersection point	y, in.	ȳ, in.
I	1		0	0.047
	2			.118
	3			.189
	5			1.604
	9			2.667
	12			3.423
	17			3.905
	18			3.940
	19		↓	3.976
II		II-D	-.466	.047
		II-O		.118
		II-N		.189
		II-B		1.023
		II-F		1.207
		II-L		1.357
		II-G		2.000
		II-K		2.281
		II-H		2.562
		II-T		2.905
		II-U		2.940
		II-J	↓	2.976
III		III-D	-.933	.047
		III-O		.118
		III-N		.189
		III-F		.811
		III-K		1.140
		III-G		1.333
		III-H		1.704
		III-T		1.905
		III-U		1.941
		III-J	↓	1.976
IV		IV-D	-1.399	.047
		IV-O		.118
		IV-N		.189
		IV-F		.415
		IV-G		.667
		IV-H		.845
		IV-T		.905
		IV-U		.941
		IV-J	↓	.976
V		V-E	.466	.047
		V-P		.118
		V-Q		.189
		V-C		1.023
		V-M		1.207
		V-O		1.357
		V-L		2.000
		V-H		2.281
		V-K		2.562
		V-T		2.905
		V-U		2.940
		V-J	↓	2.976
VI		VI-E	.933	.047
		VI-P		.118
		VI-Q		.189
		VI-M		.811
		VI-H		1.140
		VI-L		1.333
		VI-K		1.704
		VI-T		1.905
		VI-U		1.941
		VI-J	↓	1.976
VII		VII-E	1.399	.047
		VII-P		.118
		VII-Q		.189
		VII-M		.415
		VII-L		.667
		VII-K		.845
		VII-T		.905
		VII-U		.941
		VII-J	↓	.976

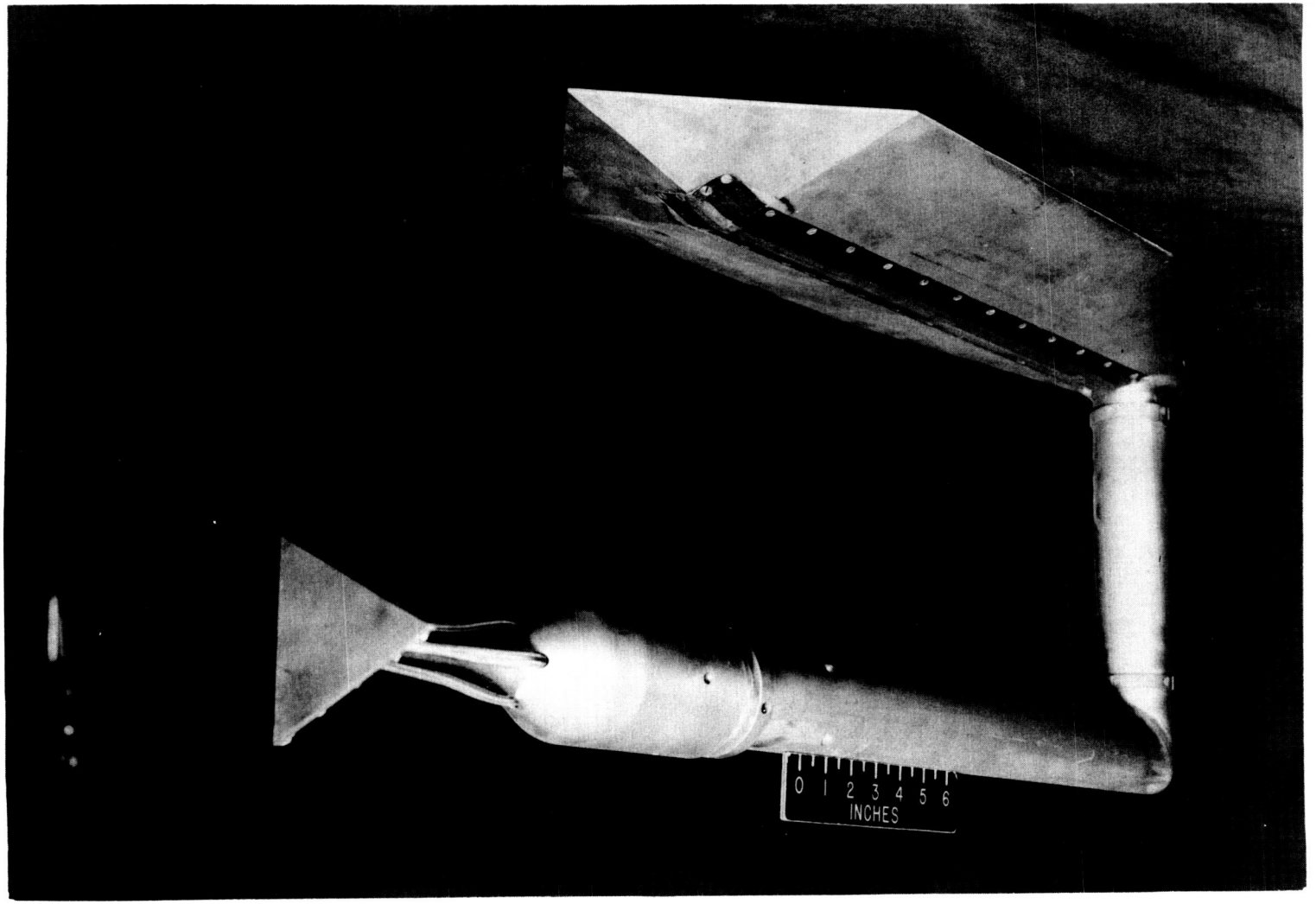

Figure 1.- Photograph of model on gooseneck support system. L-61-1204

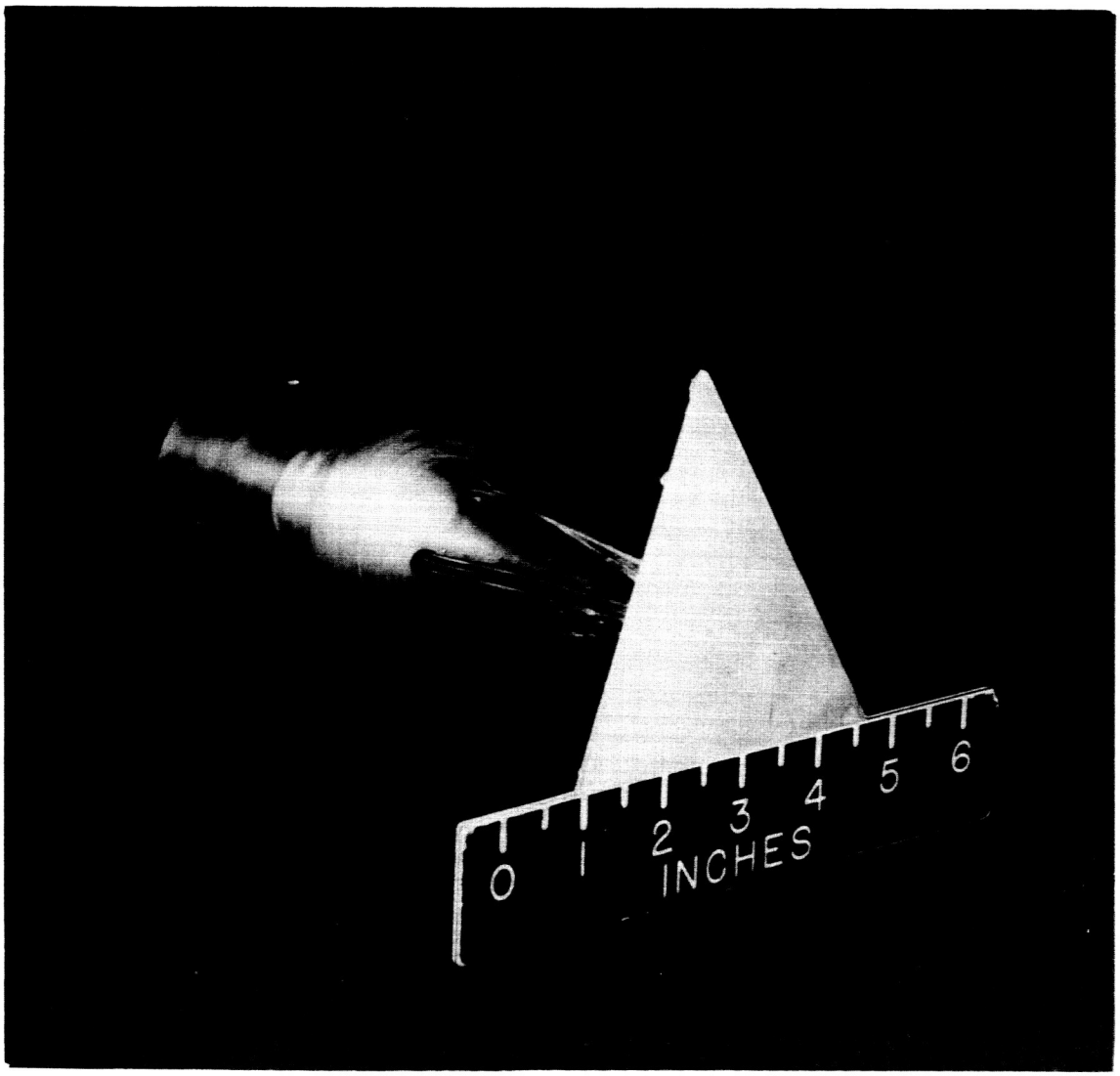

Figure 2.- Photograph of model. L-61-1205

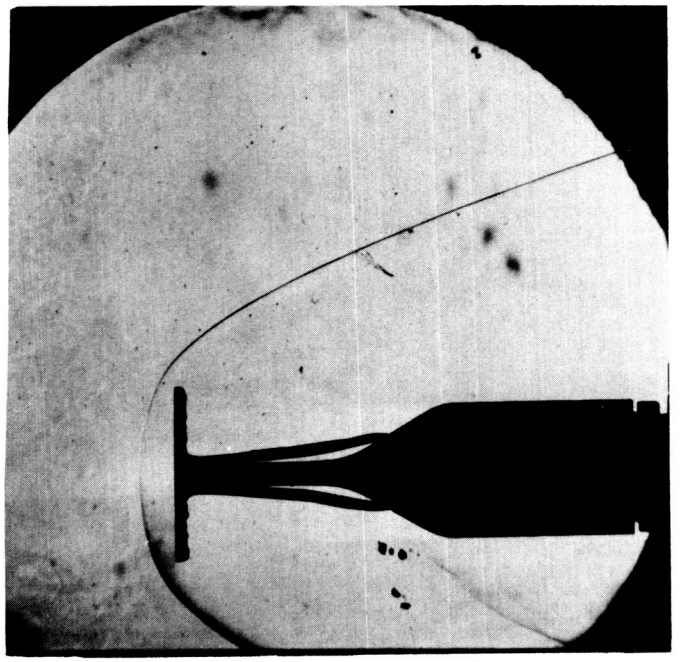

(a) Angle-of-attack attitude.

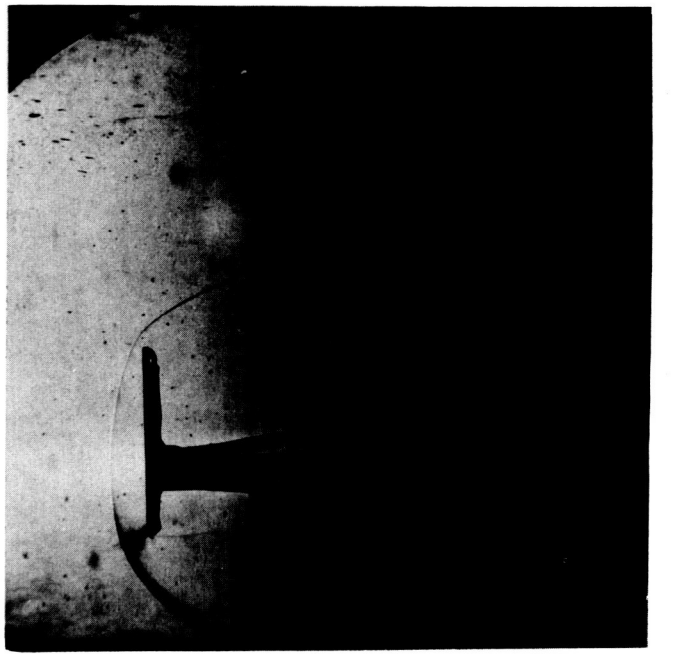

(b) Angle-of-roll attitude. L-62-2090

Figure 3.- Typical schlieren photographs.

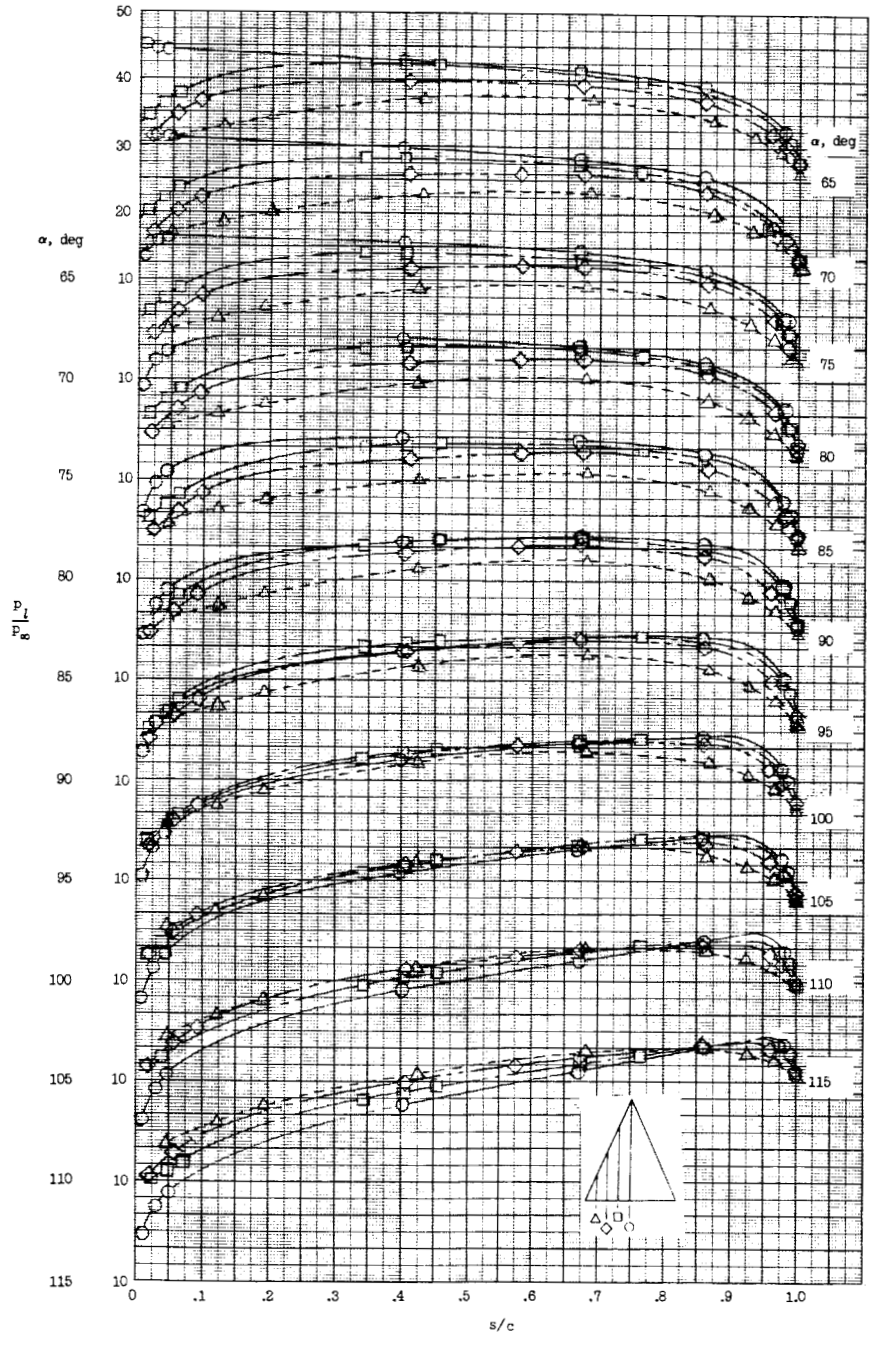

(a) For various angles of attack.

Figure 4.- Pressure distributions along equally spaced chord lines. Tick marks indicate modified Newtonian theory.

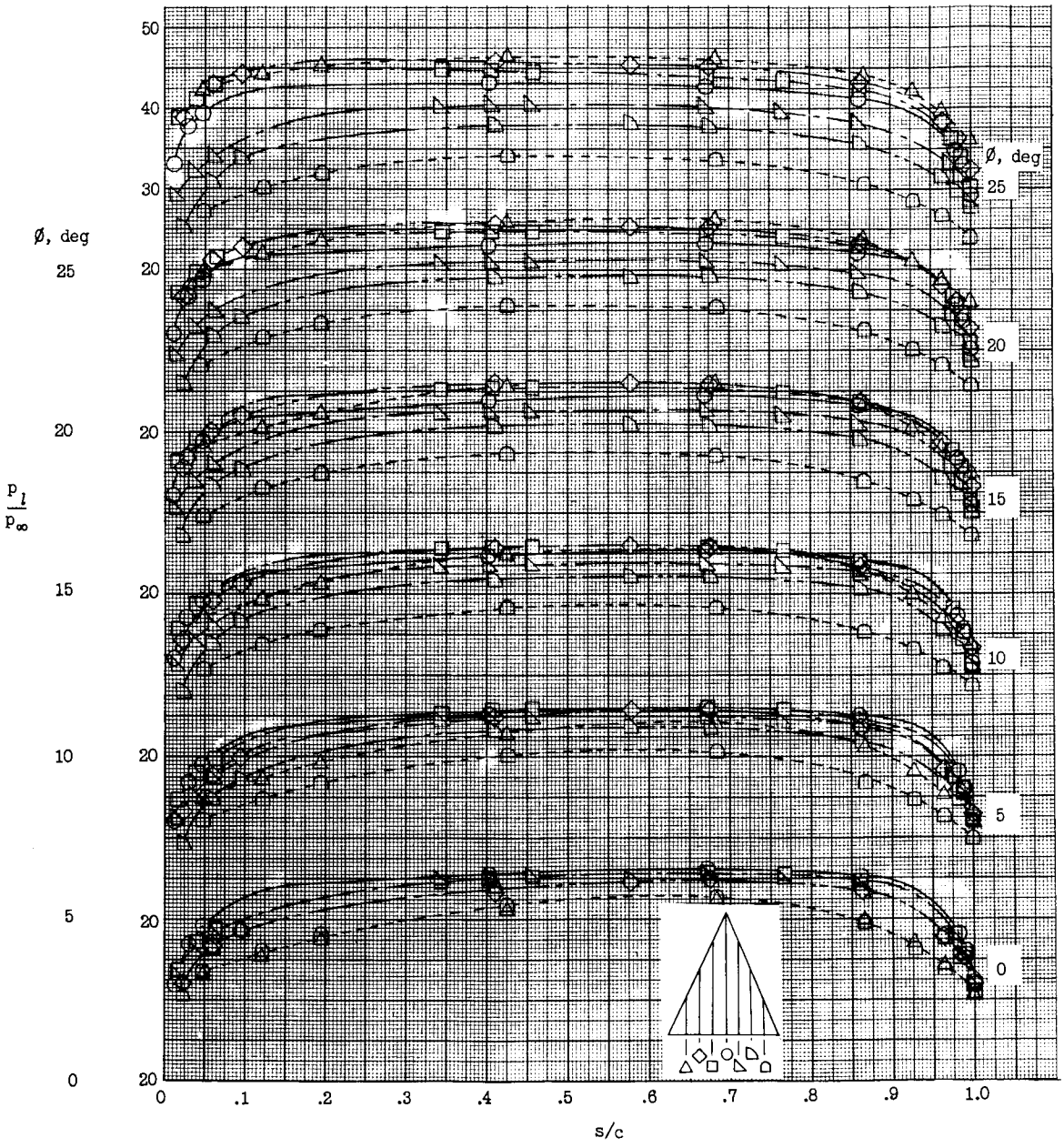

(b) For various angles of roll at a 90° angle of attack.

Figure 4.- Concluded.

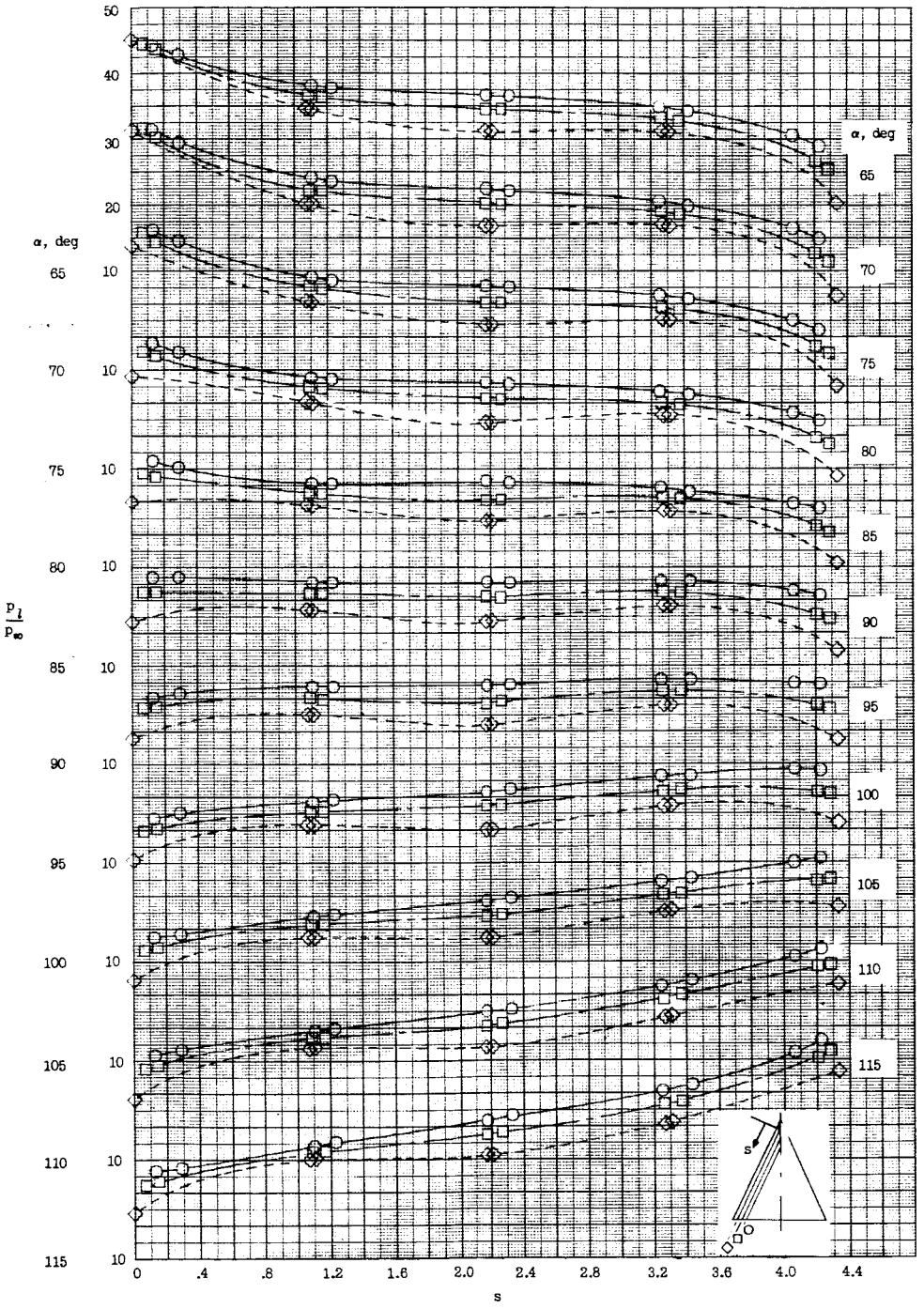

(a) For various angles of attack.

Figure 5.- Pressure distributions along rays parallel to the leading edge.

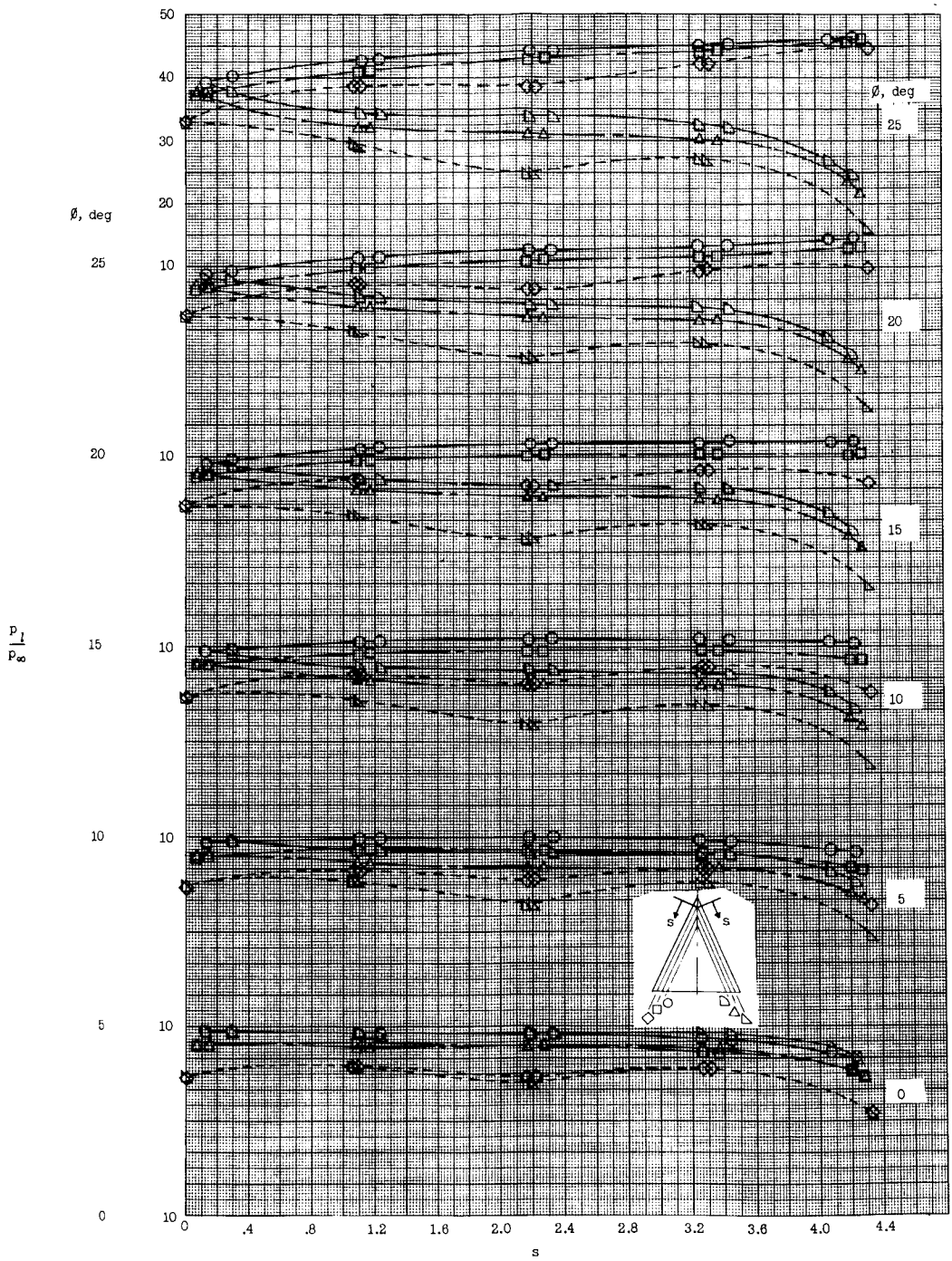

(b) For various angles of roll at a 90° angle of attack.

Figure 5.- Concluded.

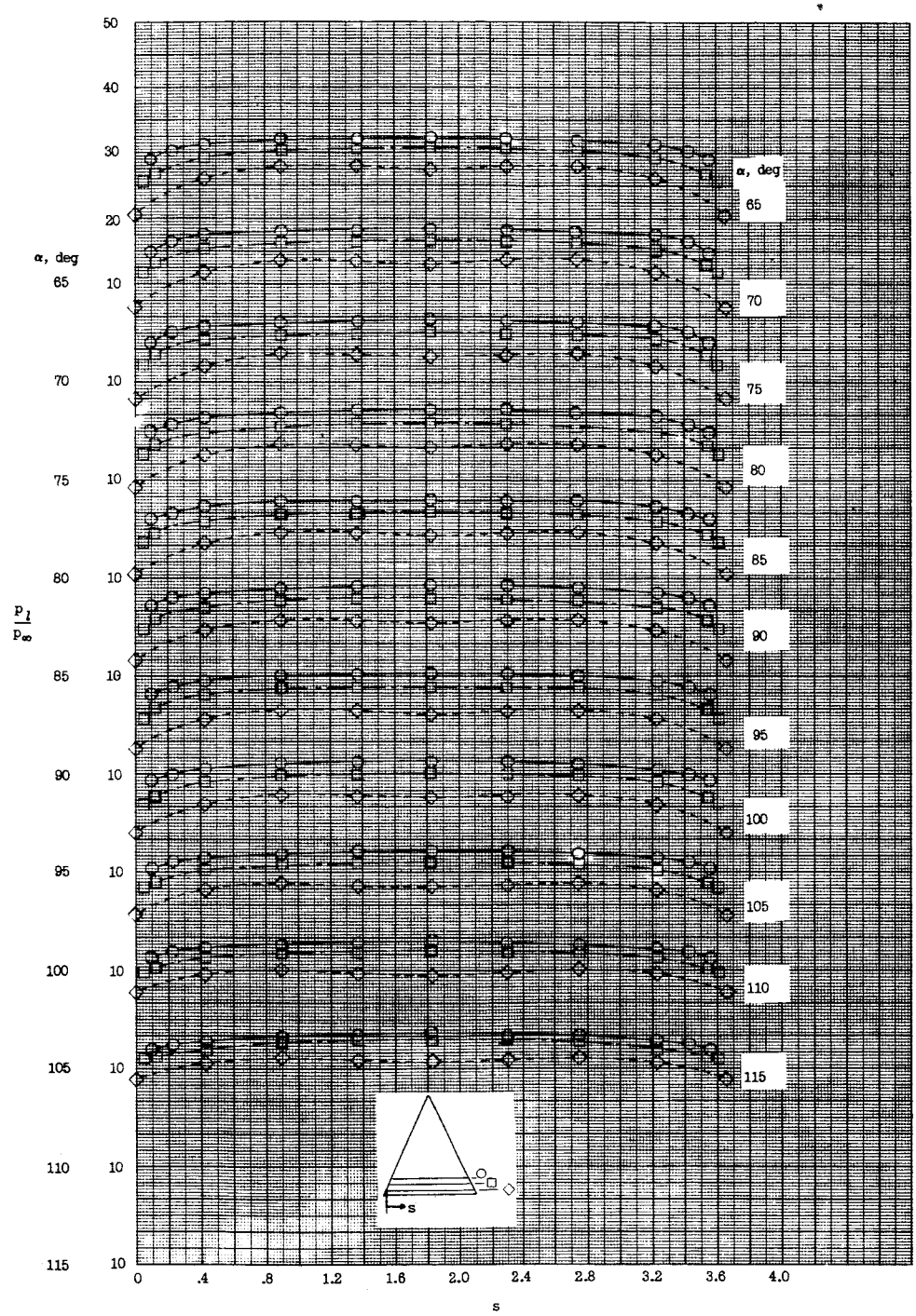

(a) For various angles of attack.

Figure 6.- Pressure distributions along rays parallel to the trailing edge.

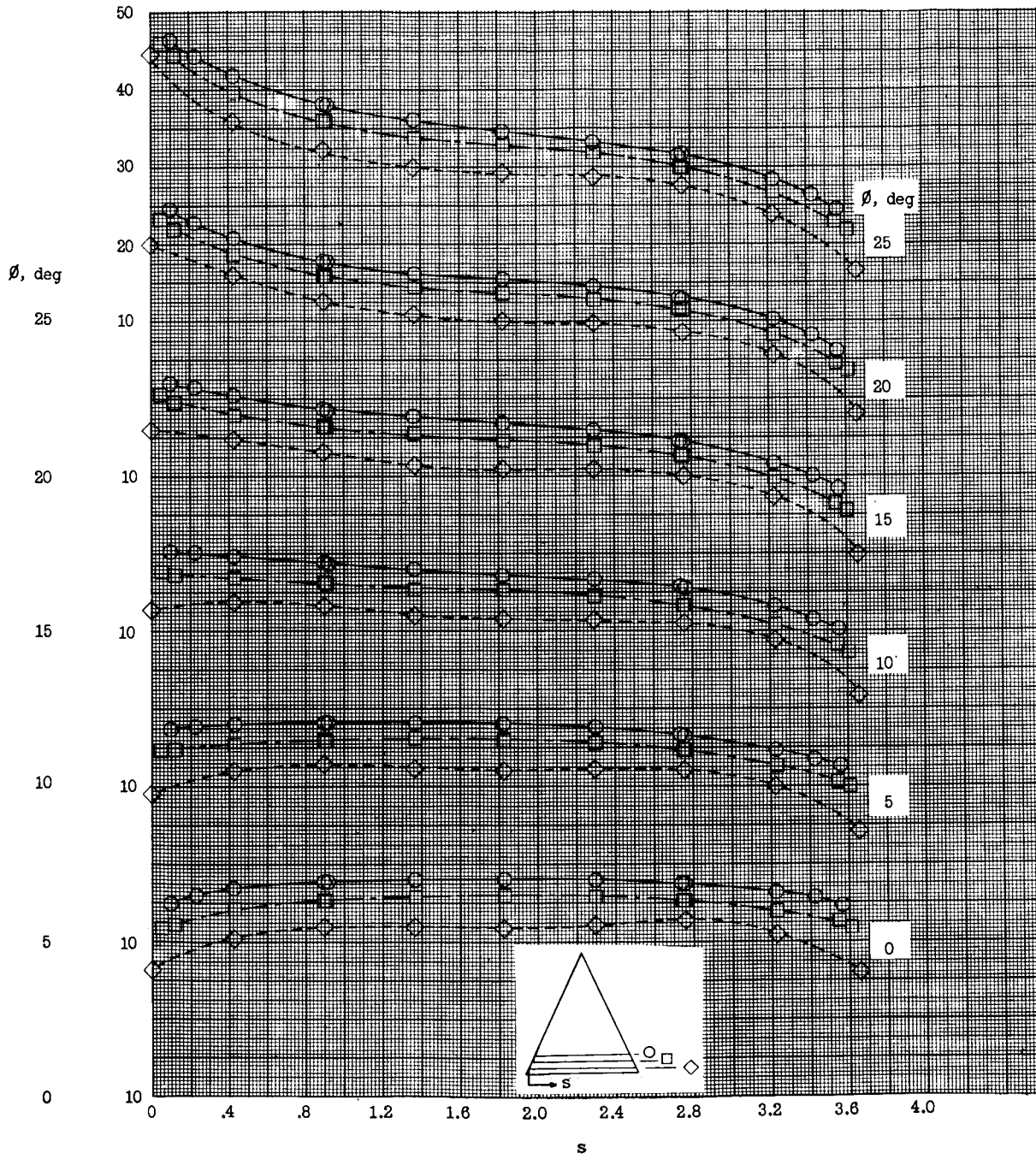

(b) For various angles of roll at a 90° angle of attack.

Figure 6.- Concluded.

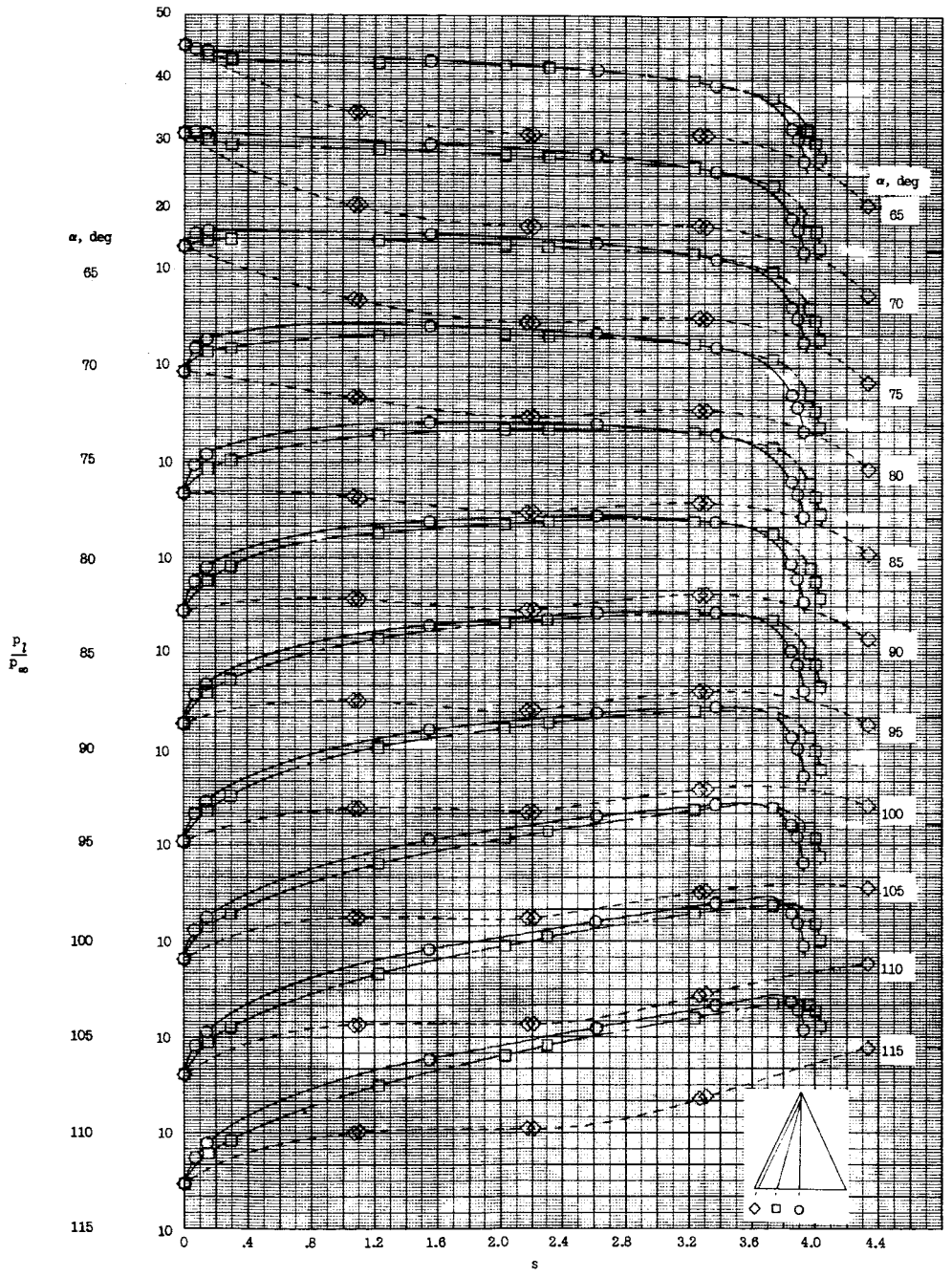

(a) For various angles of attack.

Figure 7.- Radial pressure distributions emanating from the apex orifice. Tick marks indicate modified Newtonian theory.

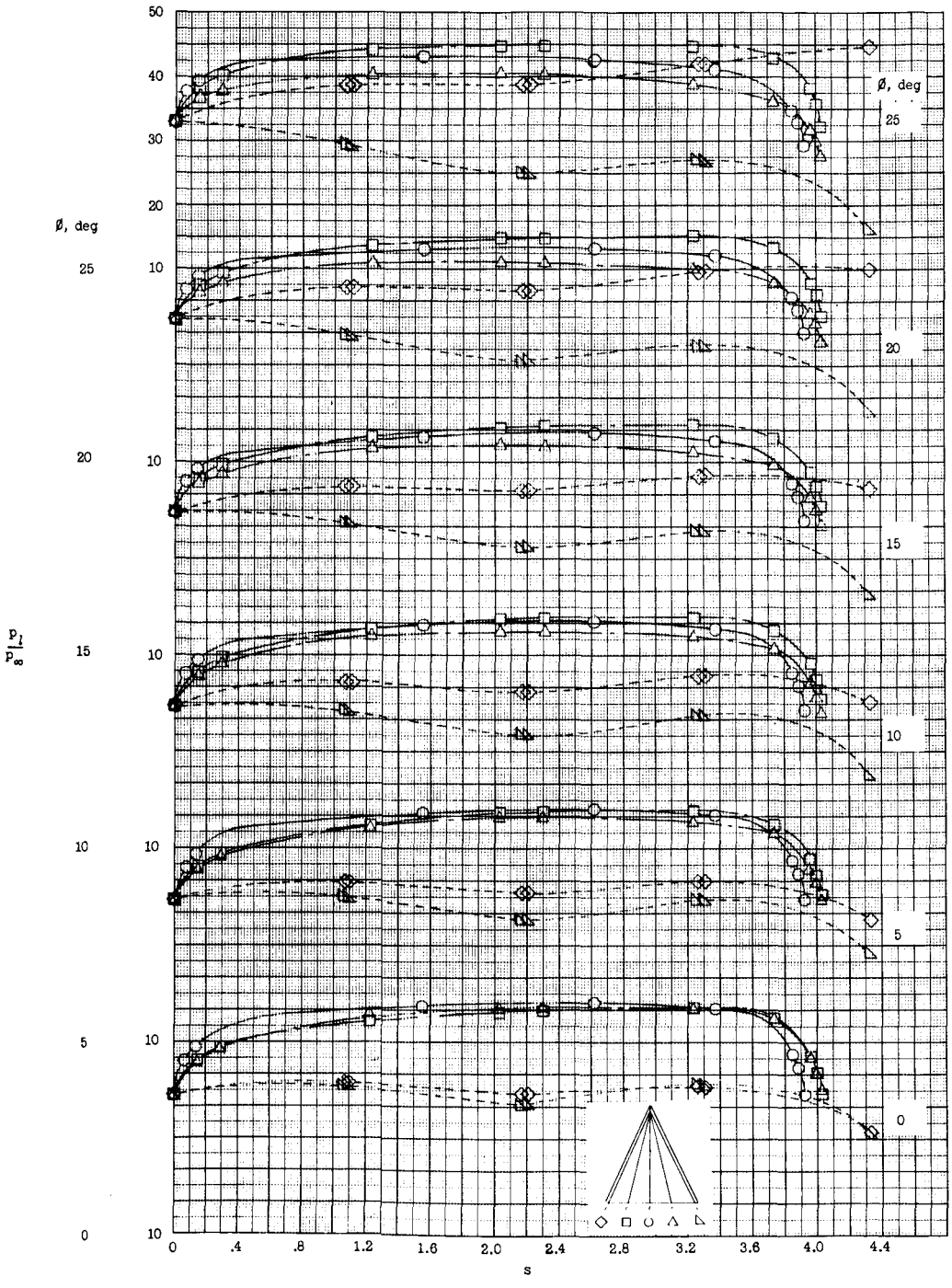

(b) For various angles of roll at a 90° angle of attack.

Figure 7.- Concluded.

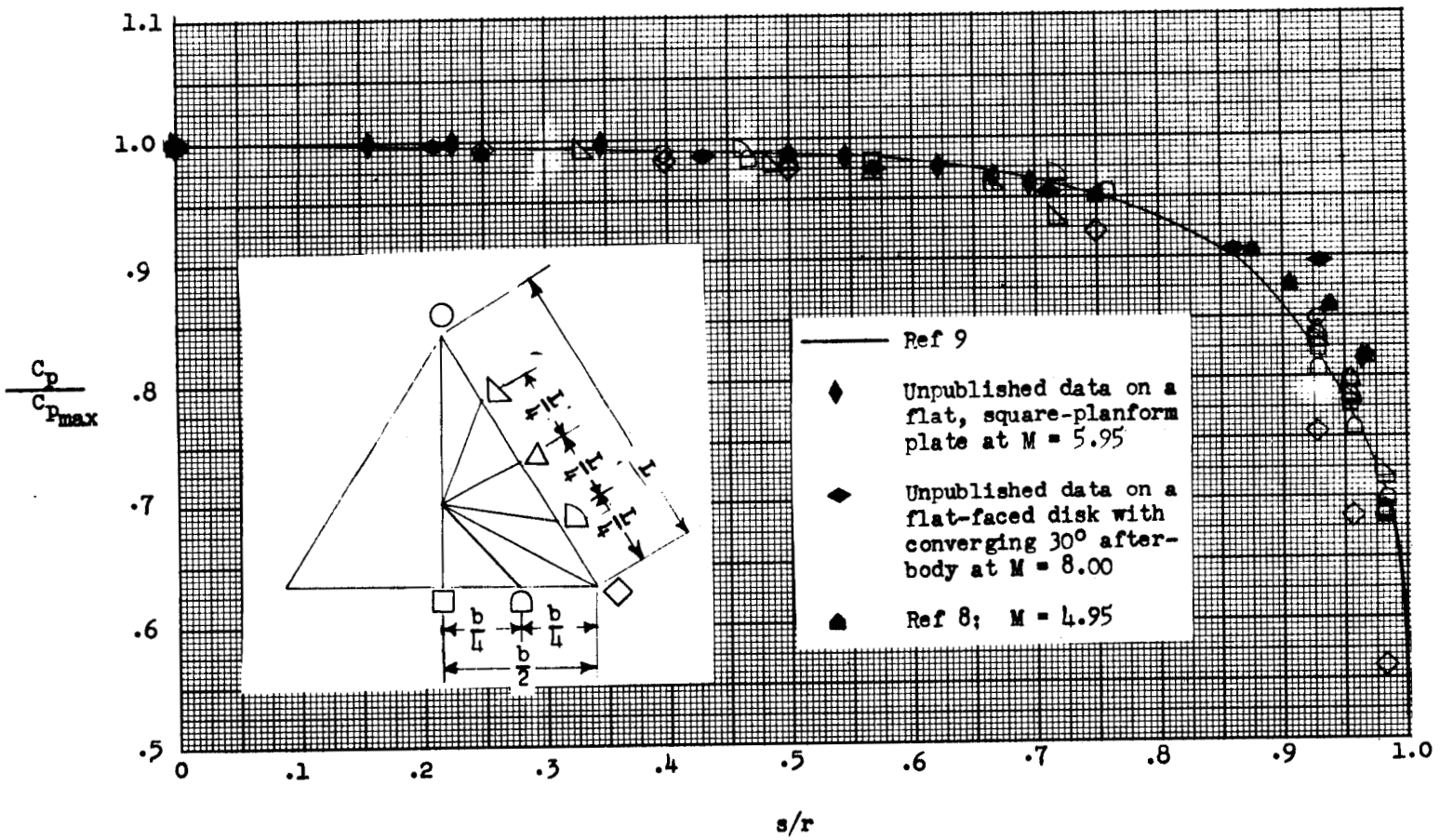

Figure 8.- Nondimensionalized correlation of pressures at a 90° angle of attack in a radial distribution emanating from the centroid of the model.

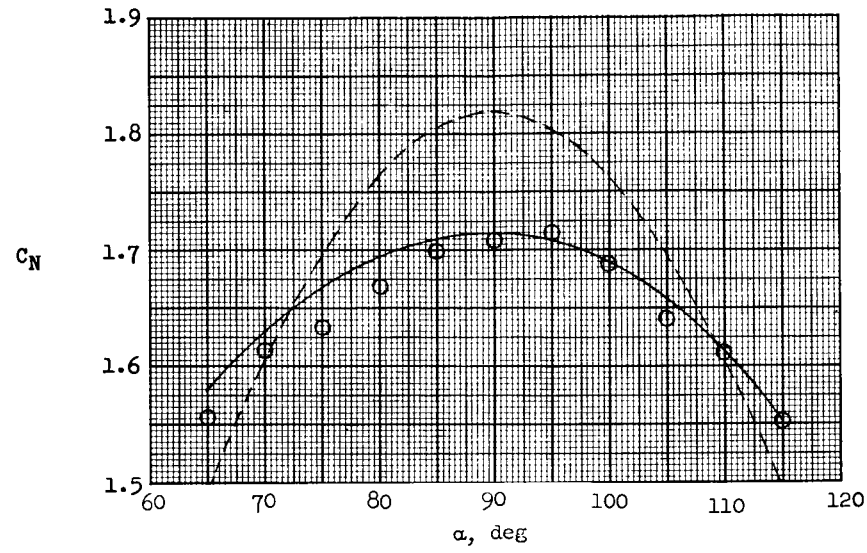

(a) Angle of attack.

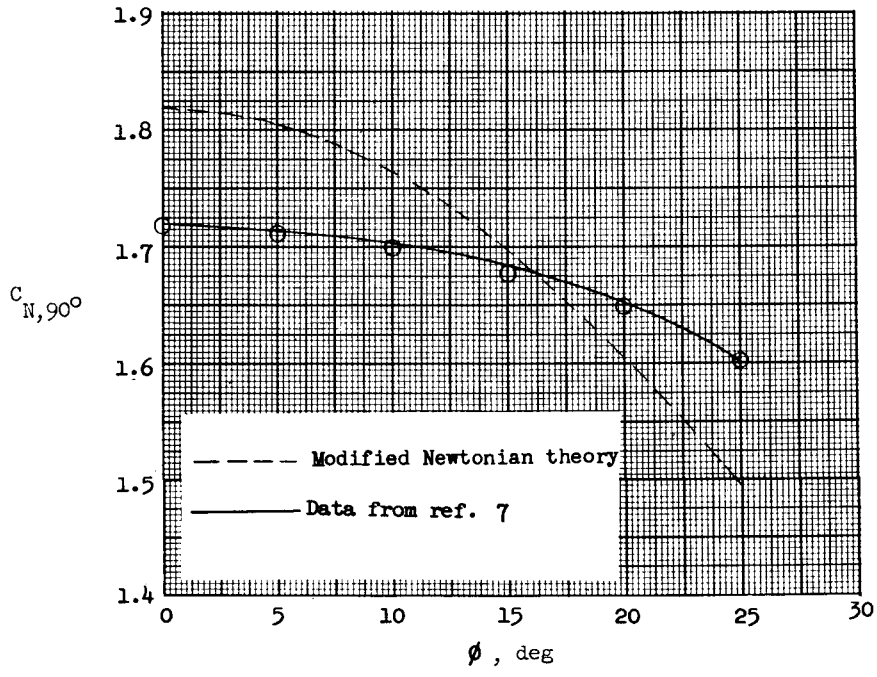

(b) For various angles of roll at a 90° angle of attack.

Figure 9.- A comparison of C_N and $C_{N,90^o}$ with modified Newtonian theory. $C_{p,max} = 1.818$.

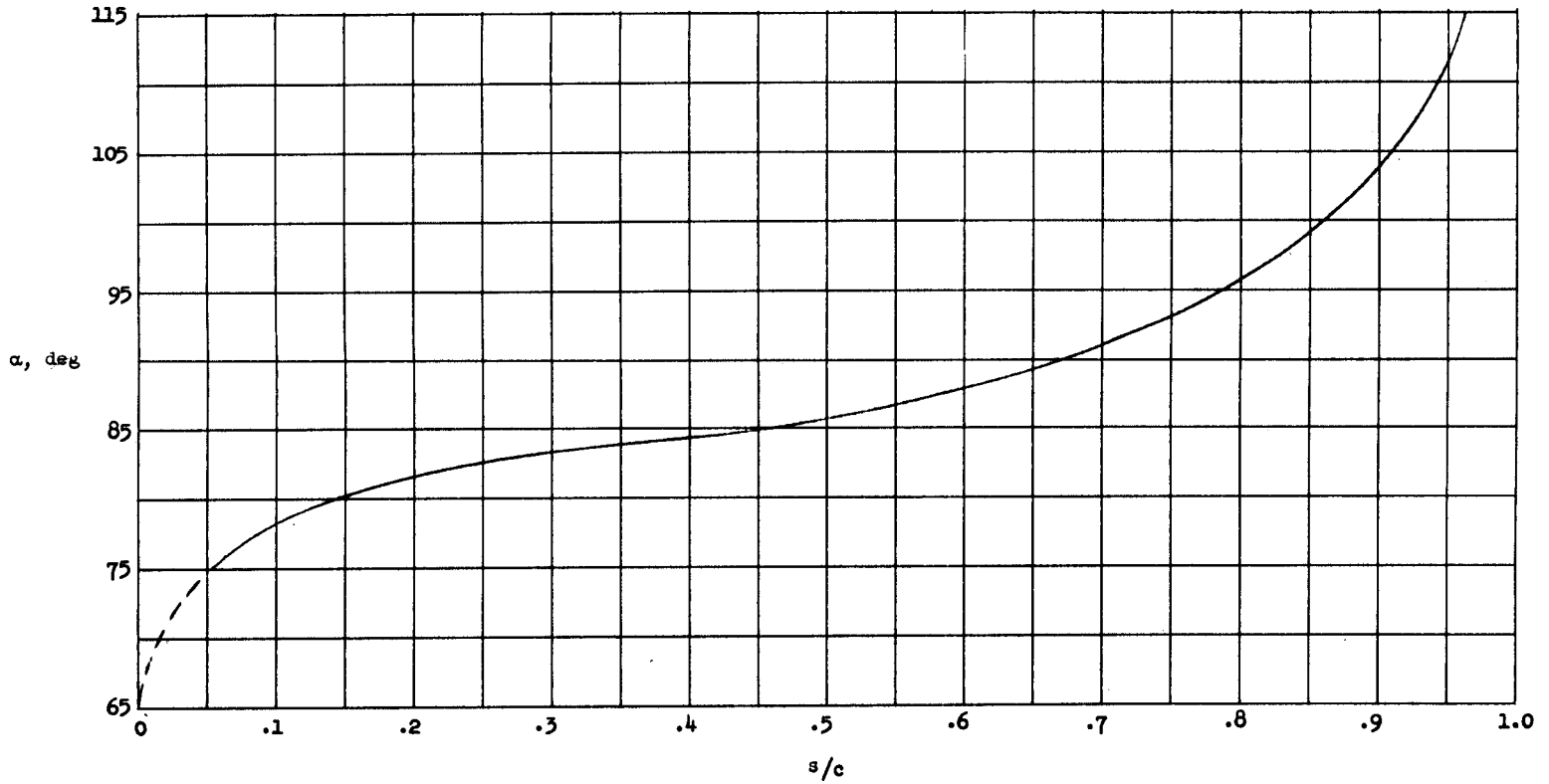

Figure 10.- Stagnation-point shift along root chord with angle of attack.

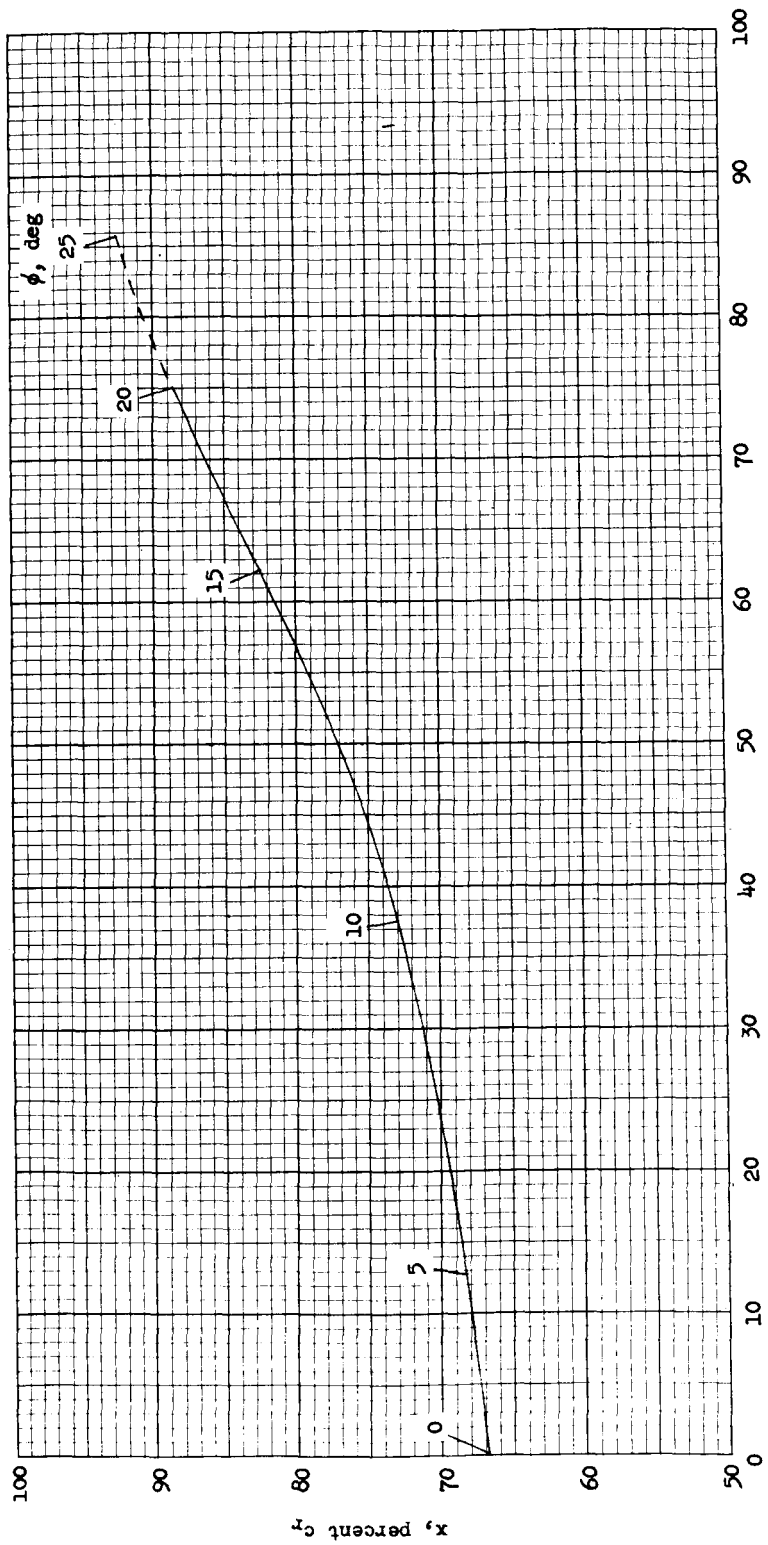

Figure 11.- Stagnation-point movement with angle of roll at a 90° angle of attack.

L-1613